POLYOXOMETALATES

Open Access
RESEARCH ARTICLE

Dual-active-site PDA@PW_{12} microspheres for high-efficiency uranium extraction via synergistic complexation and reduction

Yu Liu, Limin Zhang, Donghui Cui, Xue Yang, Xiao Liang, Keyu Chen, and Fengyan Li

Key Laboratory of Polyoxometalate and Reticular Material Chemistry of Ministry of Education, College of Chemistry, Northeast Normal University, Changchun 130024, China

Cite This: *Polyoxometalates*, **2026**, *5*, 9140119

Read Online

ABSTRACT: In this study, polydopamine@phosphotungstic acid composite microspheres for efficient uranium adsorption were successfully prepared through the *in situ* copolymerization of dopamine and phosphotungstic acid. Characterization results showed that the incorporation of phosphotungstic acid inhibited the agglomeration of polydopamine and increased the specific surface area to 48.07 m^2/g while simultaneously generating W^{5+} active species through electron transfer. The prepared material achieved a maximum uranium adsorption capacity of 720.1 mg/g at pH = 5 and 318 K, with the adsorption following the pseudo-second-order kinetic model and Langmuir isotherm model, indicating spontaneous monolayer chemisorption. Mechanistic investigations confirmed that uranium adsorption occurred through the synergistic effect of surface complexation with functional groups (–OH/–NH_2) and the reduction of U(VI) to U(IV) by W^{5+} species. The composite maintained 93.3% desorption efficiency after five adsorption–desorption cycles and exhibited excellent selectivity toward U(VI). Thus, this work provides a promising strategy for the development of high-performance uranium adsorbents.

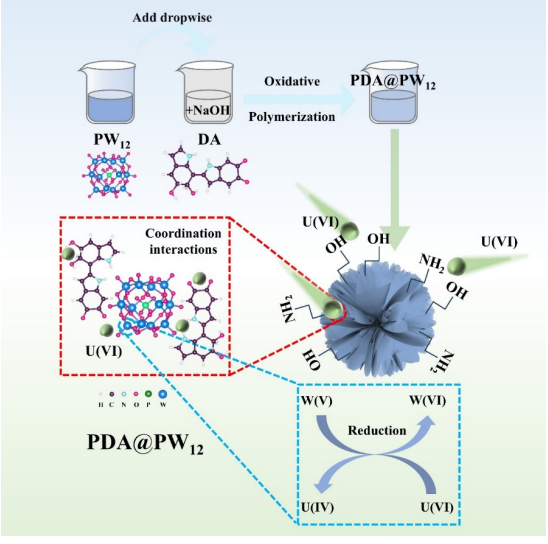

KEYWORDS: polydopamine, polyoxometalates, adsorption, uranium

1 Introduction

Global energy demand steadily rises alongside the accelerated transition to carbon neutrality, positioning nuclear power as an increasingly prominent strategic, clean, and efficient base-load energy source [1]. Uranium serves as a key element for nuclear power generation. However, uranium-containing wastewater generated during the nuclear fuel cycle and nuclear accident remediation poses serious threats to ecosystems and human health because of its radioactivity and chemical toxicity [2]. Simultaneously, seawater contains approximately 4.5 billion tons of uranium resources, making their efficient extraction strategically important for ensuring the sustainable development of nuclear energy [3]. Therefore, the development of highly efficient and selective uranium adsorption technologies is crucial for environmental remediation and resource recovery [4].

Received: December 8, 2025; **Revised:** December 30, 2025
Accepted: January 18, 2026

Address correspondence to lify525@nenu.edu.cn

https://doi.org/10.26599/POM.2026.9140119

Among various uranium separation methods, adsorption has been extensively studied because of its operational simplicity, low cost, and high efficiency [5, 6]. An ideal adsorbent must possess abundant active sites, excellent mass transfer efficiency, good selectivity, and practical applicability [7]. Polydopamine (PDA), a biomacromolecule inspired by mussel adhesive proteins, has shown promise in heavy metal adsorption owing to its universal substrate modification capability, mild synthesis conditions, and abundant catechol/amino functional groups on the surface [8]. Different PDA-based adsorbents have already been developed through various strategies. For instance, Huang et al. [9] have synthesized a phosphorylated composite (U6N@phos-PDA) via the secondary modification of PDA for uranium adsorption, whereas Hu's team [10] utilized PDA-modified fly ash composite electrodes to considerably enhance uranium electrosorption capacity, achieving uranium adsorption capacities of 423.23 and 416.96 mg/g, respectively. These works indicate the promising application value of PDA in uranium adsorption. However, pristine PDA materials or their conventional composites still suffer from notable limitations, including finite specific surface area, aggregation tendency, and a single adsorption mechanism, which are performance improvement bottlenecks [11].

Polyoxometalates (POMs, such as phosphotungstic acid) are a

class of metal-oxo cluster anions with well-defined structures [12–14]. Their high negative charge density and reversible redox properties result in their strong coordination and reduction capabilities toward uranyl ions (UO_2^{2+}) [15, 16]. Nevertheless, the inherent drawbacks of POMs, such as leaching in aqueous phases and difficult recovery, remain major obstacles for their application as adsorbents [17, 18]. Notably, although both PDA and POMs exhibit unique advantages in uranium adsorption, to the best of our knowledge, no studies have been reported on the preparation of high-performance uranium adsorbents from PDA and POMs to leverage their synergistic effects.

Herein, a novel composite material integrating PDA with POMs is proposed for uranyl ion adsorption. The prepared adsorbent synergistically combines the benefits of PDA and POMs, with PDA serving as a stable carrier for POMs, preventing their leaching and addressing recovery challenges, and providing functional groups as additional adsorption sites [19, 20]. The incorporation of POMs inhibited PDA agglomeration, increased specific surface area, and, owing to their unique electron "sponge" character, potentially induced the reductive immobilization of U(VI) via electron transfer, thereby overcoming the limitations of conventional adsorption mechanisms relying solely on surface complexation [21, 22]. Herein, a series of PDA@POM composite microspheres was successfully prepared through the *in situ* copolymerization of dopamine and phosphotungstic acid ($H_3PW_{12}O_{40}$; PW_{12}), with PDA@PW_{12} identified as the optimal material. Multiple characterization techniques confirmed strong electron interactions between PDA and PW_{12}, with PW_{12} acting as an "electron sponge" to induce p-type doping in PDA and the partial reduction of W^{6+} to W^{5+}. The U(VI) adsorption performance, selectivity, and cyclic stability of the proposed material under various conditions were systematically evaluated. Furthermore, adsorption experiments, X-ray photoelectron spectroscopy (XPS), and density functional theory (DFT) calculations revealed a dual mechanism of U(VI) adsorption via synergistic "surface complexation" and "*in situ* reduction." Thus, the present work not only provides a new strategy for the design of high-performance uranium adsorbents but also fills the research gap regarding PDA–POM composites in uranium adsorption, elucidating their interfacial electronic effects and role in environmental remediation.

2 Materials and methods

2.1 Chemicals

Unless otherwise specified, all reagents were used as received without further purification. Dopamine hydrochloride (98%), PW_{12}, uranyl nitrate hexahydrate, potassium hydroxide (KOH), ethanol (C_2H_5OH), nitric acid (HNO_3), hydrochloric acid (HCl), and Arsenazo III were purchased from Macklin.

2.2 Preparation of PDA

A solution of dopamine hydrochloride (150 mg) in water (10 mL) was prepared in a 25-mL beaker. To this solution, an aqueous solution of KOH (42 mg in 10 mL, prepared separately in another 25-mL beaker) was added, followed by stirring for 12 h at ambient temperature. The resulting black precipitate was collected through filtration, thoroughly washed with deionized water and ethanol, and dried under vacuum at 60 °C.

2.3 Preparation of PDA@PW_{12}

As shown in Fig. 1, dopamine hydrochloride (150 mg) was dissolved in 10 mL of deionized water in a 25-mL beaker. To this solution, 10 mL of an aqueous solution containing varying amounts of PW_{12} (37.5, 64.0, 100.0, and 150.0 mg) was added, followed by the addition of 10 mL of an aqueous KOH solution (42 mg) prepared separately in another 25-mL beaker. The mixture was stirred for 12 h under a nitrogen atmosphere. The resulting green precipitate was collected through filtration, thoroughly washed with deionized water and ethanol, and dried under vacuum at 60 °C. The obtained products with different PW_{12} loadings were designated as PDA@20%PW_{12}, PDA@30%PW_{12}, PDA@40%PW_{12}, and PDA@50%PW_{12}, respectively. Additionally, PDA composites with different POMs were synthesized: PDA@PMo_{12}, PDA@P_2W_{18}, and PDA@SiW_{12}.

2.4 Batch adsorption experiments

A stock solution of U(VI) (500 mg/L) was prepared by dissolving 0.105 g of uranyl nitrate hexahydrate ($UO_2(NO_3)_2{\cdot}6H_2O$) in approximately 20 mL of deionized water, followed by dilution to 100 mL in a volumetric flask. The solution was stored in the dark prior to use. Working solutions of desired concentrations were obtained via further dilution with deionized water. In batch adsorption experiments, 10.0 mg of PDA@PW_{12} was added to 50.0 mL of U(VI) solution with initial concentrations of 25.0–1275.0 mg/L for adsorption kinetics tests. The solution was then thoroughly shaken at 298 K and 150 rpm to ensure that the adsorption equilibrium was reached. Adsorption isotherms were measured at 298, 308, and 318 K. To investigate the effect of pH on adsorption performance, the initial pH of the U(VI) solution was adjusted through the addition of 0.1 mol/L HNO_3 or NaOH

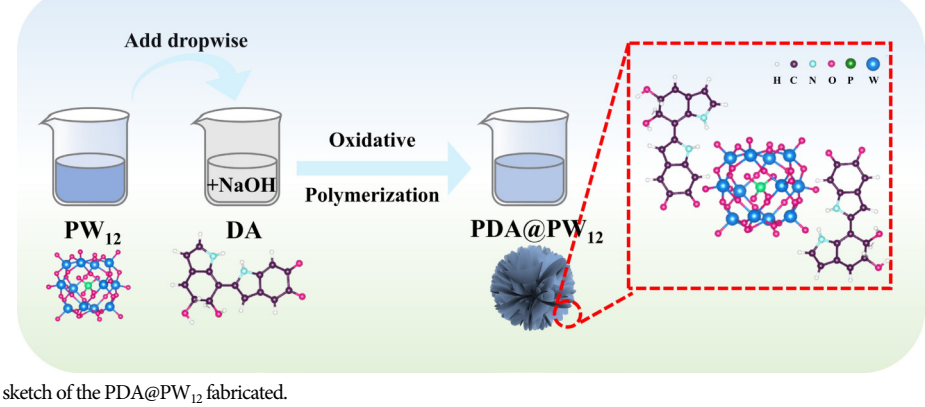

Figure 1 Diagrammatic sketch of the PDA@PW_{12} fabricated.

solutions. In the adsorption kinetics and isotherm tests, the initial pH of all U(VI) solutions was adjusted to 5.0. Various competing ions were quantitatively introduced into the system to study their impact on adsorption performance and selectivity. The equilibrium adsorption capacity for U(VI) was accurately determined by measuring the residual concentration of U(VI) post-adsorption.

3 Results and discussion

3.1 Characterization of PDA@PW_{12}

The structure and morphology of the optimized PDA@PW_{12} composite (with a PW_{12} loading of 40.0 wt.%) were characterized. The results of scanning electron microscopy (SEM) indicated that pristine PDA consisted of uniform agglomerated irregular particles with an average size of approximately 300 nm (Fig. 2(a)), whereas PDA@PW_{12} formed nanospherical structures with diameters of around 4 μm (Fig. 2(b)). In this composite system, PDA functioned as a coupling agent, providing both surface coating capability and the ability to link PW_{12} molecules [23]. The composite material was synthesized through the *in situ* polymerization of dopamine and PW_{12} under stirring, where the amino and hydroxyl groups of dopamine molecules formed hydrogen bonds with the oxygen atoms in PW_{12} [24]. Despite the considerable increase in particle size, the specific surface area of PDA@PW_{12} did not decrease. Brunauer–Emmett–Teller measurements revealed specific surface areas of 13.876 m^2/g for PDA, 17.359 m^2/g for PW_{12}, and 48.069 m^2/g for PDA@PW_{12} (Fig. S1 in the Electronic Supplementary Material (ESM)). These results were primarily attributed to the introduction of PW_{12}, which effectively inhibited the agglomeration of PDA, considerably increasing the specific surface area of the composite material and providing more active sites for U(VI) adsorption [25]. Furthermore, elemental maps of PDA@PW_{12} indicate a homogeneous distribution of C, O, N, W, and P, further confirming the successful preparation of the composite material (Fig. 2(c)).

The synthesized samples were characterized using powder X-ray diffraction (PXRD) for phase analysis. As shown in Fig. 3(a), the characteristic diffraction peaks of PW_{12} agree well with both simulated and experimental results, confirming its high phase purity [26]. In the XRD pattern of the PDA@PW_{12} composite microspheres, the characteristic peaks of PW_{12} are clearly visible without notable changes in position or intensity, indicating that the crystalline structure of PW_{12} maintained during the composite formation, confirming the successful integration of PDA with PW_{12}.

The functional group composition of the PDA@PW_{12} composite material was analyzed using Fourier transform infrared (FTIR) spectroscopy (Fig. 3(b)). The obtained spectrum indicates that the introduction of PW_{12} substantially improved the infrared absorption band profile of PDA. With increasing PW_{12} loading, the intensity and resolution of the characteristic PDA peaks gradually increased, indicating that PW_{12} promoted the formation of PDA during composite preparation. In the FTIR spectrum of PDA@PW_{12}, a series of characteristic absorption peaks for PDA are observed at 3412 cm^{-1} (O–H stretching of phenol and N–H stretching), 1630 cm^{-1} (aromatic ring stretching and N–H bending), 1518 cm^{-1} (N–H scissoring), 1395 and 1291 cm^{-1} (C–O–H bending and stretching of phenol, respectively), and 1120 cm^{-1} (C–O vibration) [27]. These observations confirm the presence of abundant oxygen-containing functional groups and aromatic ring structures on the surface of PDA@PW_{12}. Additionally, FTIR characterization was performed on PDA composites with different POMs (Fig. S2 in the ESM). Characteristic absorption peaks for

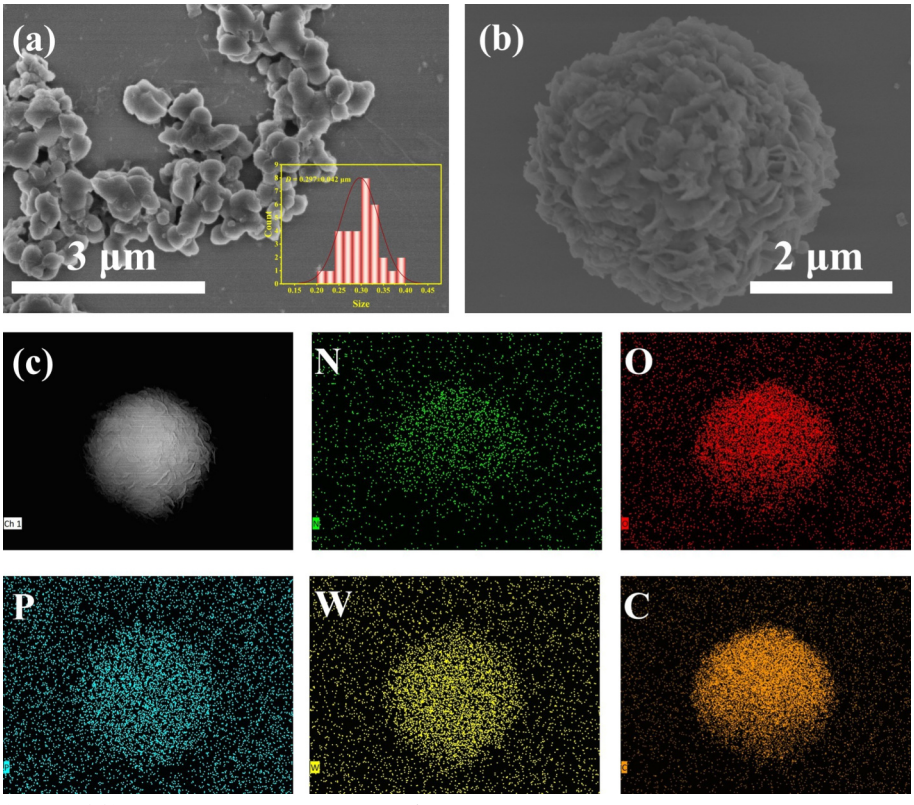

Figure 2 SEM images of (a) PDA and (b) PDA@PW_{12}. EDS mapping images of PDA@PW_{12}.

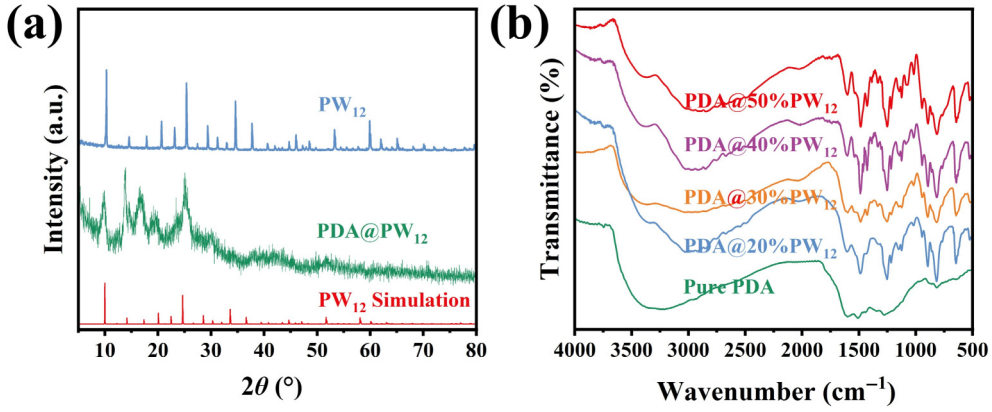

Figure 3 (a) PXRD patterns of PDA and PDA@PW_{12}. (b) FTIR spectra of PDA and PDA composites with different PW_{12} loadings.

POMs typically appear in the region below 1150 cm^{-1}, with the relevant peak positions clearly marked in the figure [28].

To investigate the changes in the chemical states of elements and electronic structure during the composite formation between PDA and PW_{12}, the materials were systematically characterized using XPS. The XPS survey spectrum (Fig. S3 in the ESM) confirms the presence of C, N, O, P, and W in PDA@PW_{12}, indicating the successful preparation of the composite material. Deconvoluted C 1s spectrum (Fig. 4(a)) reveals that the characteristic peaks of pristine PDA at 284.80, 285.98, and 289.02 eV correspond to C–C, C–N/C–O, and C=O bonds [29]. After composite formation, the corresponding peaks in PDA@PW_{12} all shifted to lower binding energies (C–C: 284.78 eV; C–N/C–O: 285.95 eV; C=O: 288.95 eV). Similarly, in the N 1s spectrum (Fig. 4(b)), the original PDA peaks for =N– (399.35 eV), –NH– (400.19 eV), and –NH_2 (400.95 eV) shifted to 398.87, 400.16, and 401.13 eV, respectively, after compositing [30]. The O 1s spectrum (Fig. 4(c)) further indicates the coexistence of characteristic peaks from both components in the composite: W–O/P–O (531.31 eV) derived from PW_{12} and C=O (532.20 eV) and C–O (533.45 eV) originating from PDA [21]. All these peaks are observed at lower binding energies than those of the individual components. The systematic decreases in the binding energies of C, O, and N were attributed to the injection of electrons into PW_{12}, which functioned as an "electron sponge" storing charge. These electrons would otherwise be released through the reaction with oxygen during the polymerization of PDA. This increased the electron cloud density of the PDA framework, thereby reducing the binding energies of its core electrons. The W 4f spectrum (Fig. 4(d)) provides direct evidence for this electron transfer: pristine PW_{12} exhibits only W^{6+} doublets ($4f_{7/2}$ 35.46 eV,

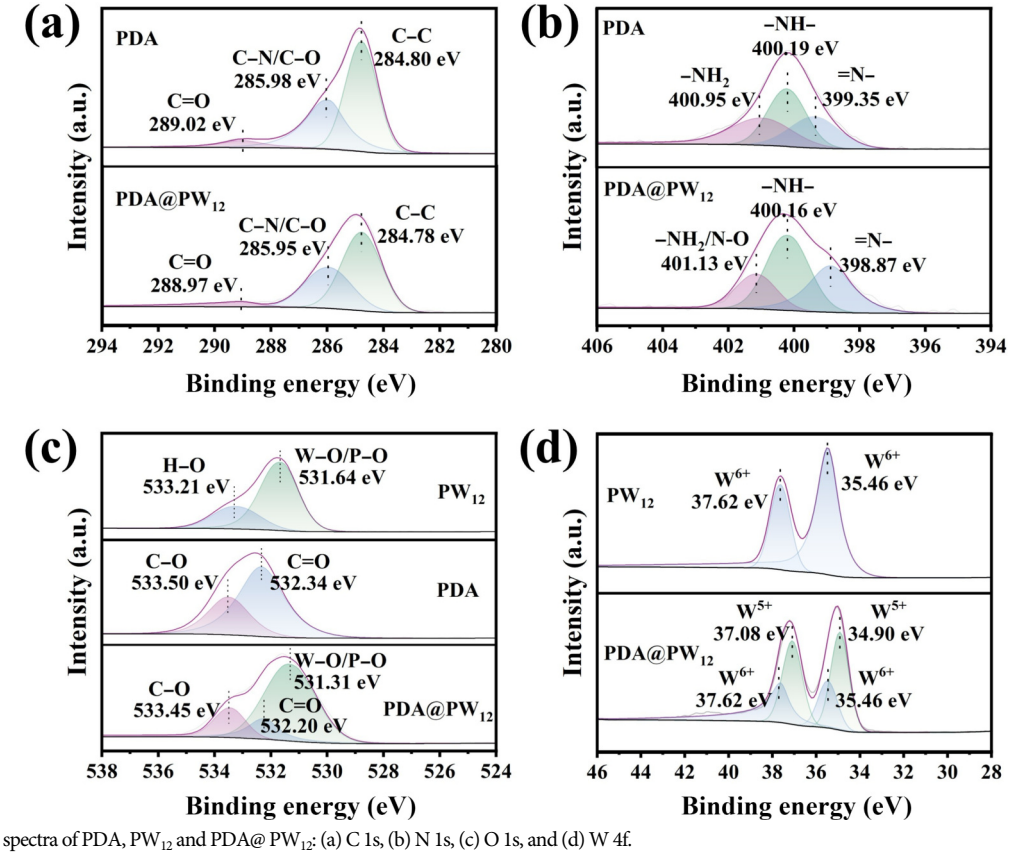

Figure 4 The XPS spectra of PDA, PW_{12} and PDA@ PW_{12}: (a) C 1s, (b) N 1s, (c) O 1s, and (d) W 4f.

$4f_{5/2}$ 37.62 eV), whereas PDA@PW_{12} shows additional distinct peaks of W^{5+} ($4f_{7/2}$ 34.90 eV, $4f_{5/2}$ 37.08 eV), confirming the partial reduction of W^{6+} during composite formation [31]. Thus, XPS results consistently show that the interactions between PDA and PW_{12} involved physical compositing and considerable electron transfer. These findings provide important mechanistic insights at the microscopic level for understanding the enhanced uranium adsorption performance of the composite material.

3.2 Adsorption performance

The present study systematically evaluated the adsorption behavior of PDA@PW_{12} in uranium solutions of different concentrations. By comparing the changes in uranium concentration under dark and illuminated conditions, we confirmed that the proposed material exhibits good adsorption performance but no notable photocatalytic activity (Fig. S4 in the ESM). Thus, four composite materials (PDA@PW_{12}, PDA@PMo_{12}, PDA@P_8W_{48}, and PDA@SiW_{12}) were further synthesized, and their U(VI) extraction performance under identical conditions was systematically compared. As shown in Fig. S5 in the ESM, at an initial uranium concentration of 100 mg/L, pH = 5, and a solid-to-liquid ratio of 0.2 g/L, PDA@PW_{12} exhibits the optimal extraction capability, with an extraction rate of 90%. In contrast, PDA, PDA@PMo_{12}, PDA@P_8W_{48}, and PDA@SiW_{12} exhibit extraction rates of 29.12%, 46.82%, 63.45%, and 66.91%, respectively.

A series of PDA@PW_{12} materials with PW_{12} loadings of 20%–50% (w/w) was further prepared. As shown in Fig. 5(a), at a PW_{12} loading of 40.0%, the U(VI) extraction rate reached 100%. Further increasing the loading of PW_{12} resulted in a decline in extraction efficiency, which was attributed to excessive PW_{12} covering or occupying the effective adsorption sites on the PDA surface, thereby reducing their utilization efficiency. Under the same experimental conditions, the U(VI) extraction rate of PDA@40%PW_{12} is approximately 3.1 times that of unmodified PDA, indicating that compositing with PW_{12} substantially enhanced the uranium adsorption performance of the material.

3.3 Adsorption kinetics and isotherms

The kinetics of U(VI) adsorption on PDA@PW_{12} were investigated using adsorption kinetics models and the Weber–Morris intraparticle diffusion model. As shown in Fig. 5(b), during the initial rapid adsorption phase (30 min), the abundant active sites on the PDA@PW_{12} surface facilitated the fast diffusion of U(VI) from the solution to the material surface. As the reaction progressed, the surface adsorption sites gradually became saturated, and U(VI) further migrated to the PDA matrix. Subsequent adsorption primarily occurred within the internal pore structure of the material, eventually reaching equilibrium [32]. As summarized in Table 1, the pseudo-second-order kinetic model exhibits a high correlation coefficient ($R^2 > 0.998$) with the experimental data, and the calculated equilibrium adsorption capacity (q_e) agrees well with the measured value, indicating that adsorption was predominantly controlled by chemisorption. Further analysis using the Weber–Morris model (Fig. 5(c)) reveals that the adsorption of U(VI) on PDA@PW_{12} could be divided into two distinct stages. The mesopores in the material, with an average pore diameter of 3.363 nm (Fig. S1 in the ESM), are substantially larger than the hydrated diameter of the uranyl ion. This confirms that the pore channels are readily accessible for intraparticle diffusion, supporting their role in adsorption. The thickness of the boundary layer (C) is an important parameter reflecting the mass transfer characteristics in the surface region of the adsorbent in the initial diffusion stage. Typically, $C > 0$ indicates the presence of a considerable boundary layer effect, whereas geometrically irregular adsorbent surfaces may

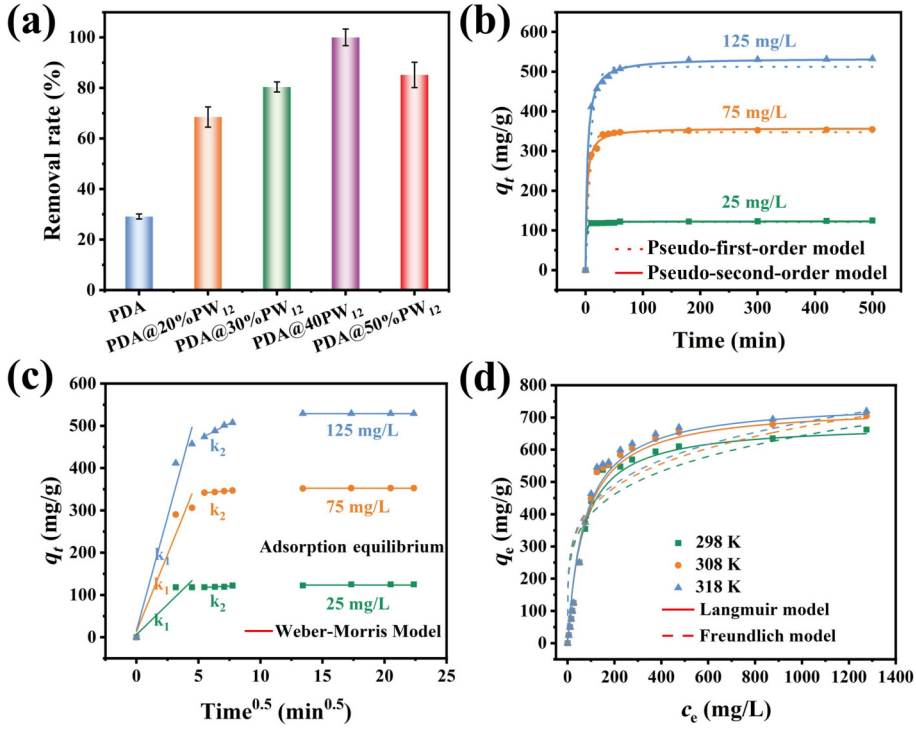

Figure 5 (a) Adsorption properties of PDA at different PW_{12} ratios (C_0 = 50 mg/L, pH = 5, m/V = 0.2 g/L), (b) pseudo-first-order and pseudo-second-order kinetics, and (c) Weber–Morris models for the adsorption process of PDA@PW_{12} toward U(VI) (pH = 5, m/V = 0.2 g/L). (d) The adsorption isotherms of PDA@PW_{12} at 298–318 K and fitted results of Langmuir and Freundlich models (pH = 5, m/V = 0.2 g/L).

Table 1 Pseudo-first-order, pseudo-second-order kinetic models and Weber-Morris model fitting parameters of PDA@PW_{12} toward U(VI) adsorption

Model	Parameter	U(VI) concentration (mg/L)		
		25	75	125
Pseudo-first-order	k_1 (min^{-1})	0.346	0.154	0.117
	q_e (mg/g)	121.315	347.224	512.281
	R^2	0.996	0.986	0.971
Pseudo-second-order	k_2 (g/(mg·min))	1.45×10^{-2}	1.17×10^{-3}	5.84×10^{-4}
	q_e (mg/g)	122.701	357.975	533.844
	R^2	0.998	0.998	0.999
Weber–Morris	k_1 (g/(mg·min)$^{1/2}$)	28.463	72.737	107.390
	C_1	6.395	13.638	16.299
	R^2	0.919	0.942	0.961
	k_2 (g/(mg·min))	2.182	2.448	15.027
	C_2	109.539	328.022	392.720
	R^2	0.753	0.985	0.986
Experimental q_e (mg/g)		125.224	354.375	532.237

exhibit negative C values, reflecting non-uniform distributions of solution flow velocity and concentration gradients [33]. The non-zero intercepts observed in the fitted curves for each stage (Table 1), combined with the results of pore size analysis, suggest that, in addition to intraparticle diffusion, the adsorption rate is affected by other mass transfer processes.

The effects of temperature on the U(VI) adsorption performance of PDA@PW_{12} and its adsorption thermodynamics were further investigated. The experimental data were fitted and analyzed using the Langmuir and Freundlich models (Fig. 5(d)). As summarized in Table S1 in the ESM, the Langmuir model exhibits a higher correlation coefficient (R^2), indicating the homogeneous distribution of adsorption sites on the PDA@PW_{12} surface and the monolayer adsorption of U(VI). According to the fitted Langmuir model, the saturated adsorption capacity of PDA@PW_{12} for U(VI) is 750.28 mg/g at 318 K. The experimentally measured saturated adsorption capacity is 720.13 mg/g, which is higher than the values reported for most similar adsorbents (Fig. S6 in the ESM and Table 2). The adsorption capacity gradually increases with temperature, suggesting that adsorption is endothermic. The results of thermodynamic analysis based on the Van't Hoff equation (Table S2 in the ESM) show that the absolute value of the standard Gibbs free energy ($\Delta G°$) increases with temperature, whereas the standard enthalpy change ($\Delta H°$) is positive [34]. These results indicate that elevated temperatures favor the spontaneity of the adsorption reaction and further confirm the endothermic nature of the process. Furthermore, the positive value of the standard entropy change ($\Delta S°$) suggests an increase in disorder at the solid–liquid interface during adsorption.

3.4 Influencing factors

Solution pH considerably affects the U(VI) adsorption behavior of PDA@PW_{12} by regulating both the uranium speciation and the surface properties of the adsorbent [35]. The adsorption performance of PDA@PW_{12} for U(VI) was systematically investigated in the pH range of 2–9. The results (Fig. 6(a)) indicate that the adsorption capacity initially increases and then decreases with rising pH, reaching a maximum value at pH = 5. Uranium

Table 2 Adsorption capacities toward U(VI) of some composite adsorbents

Materials	q_e (mg/g)	References
PDA@PW_{12}	720.1	This work
mPDA-oxime	553.03	[37]
PDA/b-CD/CFA	537.6	[38]
GO/PDA/PAO	502.5	[39]
PDA polymer	500	[40]
U6N@phos-PDA	423.23	[9]
CFA/PDA	416.96	[10]
CNTs@H-PDA-AO	318.98	[41]
PDA/CNT	309.65	[42]
AM/PDA	250.7	[43]
HNTs@PDA	72.5	[44]
Fe_3O_4@PDA	56.39	[45]
MWCNTs@PDA@TNS	26.7	[46]

speciation indicates that under acidic conditions (pH < 5), U(VI) exists predominantly as UO_2^{2+} ions. The abundant H^+ ions in the solution at this stage compete with UO_2^{2+} for the active sites on the material surface, suppressing U(VI) adsorption and thereby reducing removal efficiency. As the pH increases to 5, the H^+ concentration decreases, and the surface charge properties of the material change. This facilitates the approach and occupation of adsorption sites by UO_2^{2+} ions, leading to the formation of stable surface complexes, maximizing the adsorption capacity. When the pH was further increased (pH > 5), U(VI) underwent gradual hydrolysis, generating hydroxylated species such as $(UO_2)_3(OH)_5^+$, $(UO_2)_4(OH)_7^+$, and $UO_2(OH)_2$ [36]. These hydrolysis products exhibit low solubility, large hydrated radii, weak diffusion mobility, and reduced affinity toward the adsorbent, complicating their effective capture and ultimately causing a decline in adsorption capacity.

Considering the complex composition of actual wastewater, which may affect the interactions between the adsorbent and U(VI) ions, the present study systematically investigated the effects of coexisting metal ions on the adsorption behavior (Fig. 6(b)). The U(VI) adsorption performance of PDA@PW_{12} in multicomponent solutions shows that the presence of concomitant metal ions slightly reduces U(VI) adsorption. This was attributed to the partial coordination of metal ions with the abundant hydroxyl groups on the PDA surface, which occupied some adsorption sites and consequently reduced the U(VI) adsorption capacity. Considering the adsorption selectivity of PDA@PW_{12} for U(VI), we observed that in mixed solutions, both the adsorption capacity and distribution coefficient for U(VI) are considerably higher than those for other metal ions (Fig. 6(c) and Table 3). This indicated the highly selective adsorption of U(VI). This selectivity likely resulted from the preferential binding of uranyl ions by surface functional groups through electrostatic attraction and chelation, whereas the adsorption of other metal ions was suppressed because of differences in their hydrated radii, charge, or coordination ability [47].

3.5 Practical application and regeneration capacity

To evaluate the practical application potential of PDA@PW_{12}, we systematically investigated its chemical stability and regeneration performance. First, the stability of the material was tested under strongly acidic conditions (pH = 1) to examine whether PDA

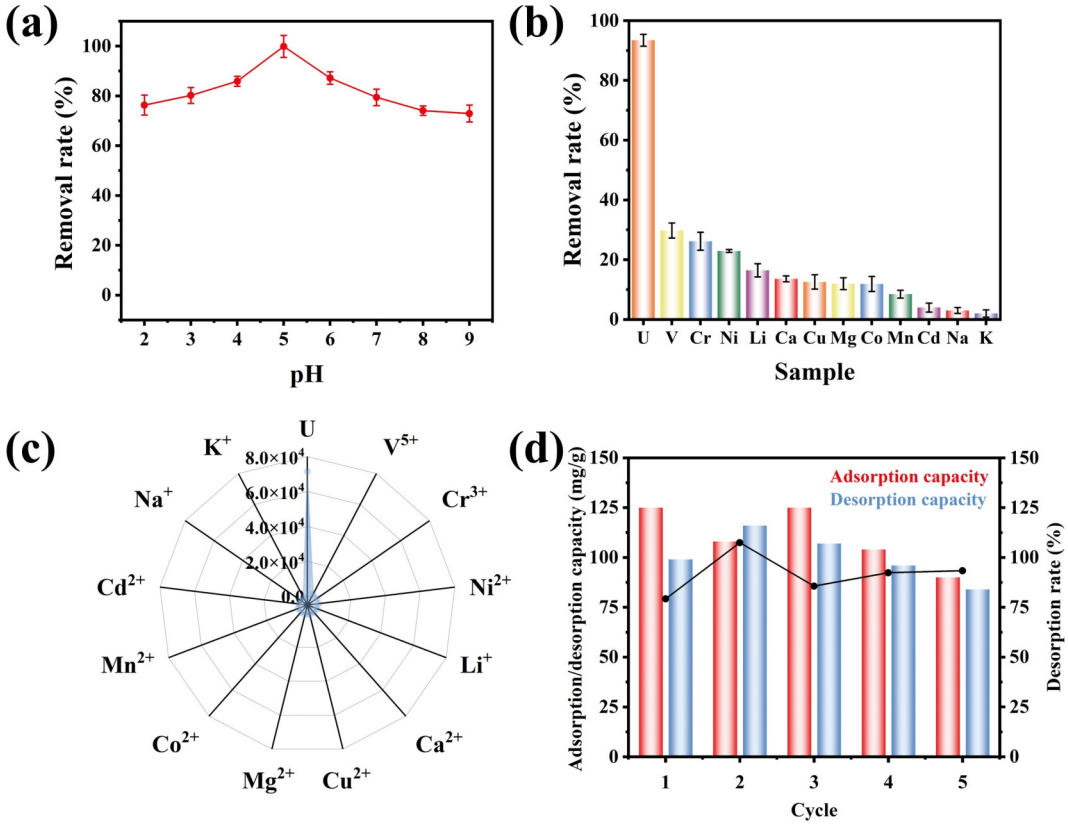

Figure 6 (a) The adsorption capacities of PDA@PW_{12} at different pH (C_0 = 50 mg/L, m/V = 0.2 g/L), (b) influences of various cations in solution on U(VI) adsorption performance (C_0 = 10 mg/L, pH = 5, m/V = 0.2 g/L), (c) adsorption distribution coefficients K_d of various cations by PDA@PW_{12} in a mixture of different ions, and (d) cyclic stability experiments of PDA@PW_{12} (C_0 = 25 mg/L, pH = 5, m/V = 0.2 g/L).

Table 3 The adsorption distribution coefficients K_d and adorption capacities of various cations by PDA@PW_{12} in a mixture

Metal ions	q_e (mg/g)	K_d (mL/g)
U	46.73	7.1×10^4
V^{5+}	14.88	2.1×10^3
Cr^{3+}	13.01	1.7×10^3
Ni^{2+}	11.46	1.4×10^2
Li^{+}	8.23	9.8×10^2
Ca^{2+}	13.57	7.8×10^2
Cu^{2+}	6.28	7.1×10^2
Mg^{2+}	5.98	6.8×10^2
Co^{2+}	5.94	6.7×10^2
Mn^{2+}	4.24	4.6×10^2
Cd^{2+}	2.08	2.0×10^2
Na^{+}	3.59	1.5×10^2
K^{+}	2.18	1.0×10^2

decomposition or PW_{12} leaching occurred. FTIR and XRD results (Fig. S9 in the ESM) indicate that the material maintained its structural integrity and composition under these conditions, without notable decomposition or loss of active components. Subsequently, using 0.1 M HCl solution as the desorption agent, adsorption–desorption cycling experiments for uranium were conducted to further evaluate the reusability of the material. After five cycles, the U(VI) adsorption capacity of the material decreased only slightly, whereas the desorption efficiency remained at 93.3% (Fig. 6(d)), demonstrating its excellent regeneration capability. The thermal stability of the materials was systematically evaluated via thermogravimetric analysis (Fig. S7 in the ESM). The results indicate that pure PDA underwent gradual decomposition with increasing temperature, exhibiting poor thermal stability. In contrast, PW_{12} shows only a minor mass loss caused by the release of crystal water while maintaining an intact framework structure, which indicates excellent thermal stability, consistent with Ref. [48]. At the same time, PDA@PW_{12} exhibits notably better thermal stability owing to the incorporation of PW_{12}, which helped retain the structural integrity and performance of the material below 350 °C. These results collectively indicate that the regenerated PDA@PW_{12} maintained excellent uranium adsorption performance. The favorable adsorption performance, thermal stability, and recyclability of the proposed material suggest its promising potential for practical applications in uranium extraction from seawater and uranium resource recovery.

3.6 Adsorption mechanism

To elucidate the adsorption mechanism of U(VI) on PDA@PW_{12}, its morphology and elemental distribution after U(VI) adsorption were investigated using scanning electron microscopy and energy-dispersive X-ray spectroscopy (EDS). As shown in Fig. S8(a) in the ESM, no notable changes are observed in either the macroscopic morphology or the crystalline structure of the material after adsorption, indicating the excellent structural stability and practical application potential of PDA@PW_{12}. The elemental maps further reveal a homogeneous distribution of uranium on the material surface, confirming the effective capture of U(VI) (Fig. S8(b) in the ESM). The adsorption mechanism was further investigated using

FTIR and XPS. The FTIR spectrum (Fig. S10(a) in the ESM) shows that a new absorption peak at 917 cm^{-1} emerges after adsorption, which was attributed to the U–O bond vibration, indicating coordination between U(VI) and the surface functional groups in the material [49]. The XRD pattern (Fig. S10(b) in the ESM) exhibits the diffraction peaks of PDA@PW_{12} before and after uranium adsorption. The intensity of the peaks is slightly lower after adsorption, while the overall peak profile is unchanged, indicating that the crystalline structure did not change during adsorption.

The adsorption mechanism of U(VI) on PDA@PW_{12} was investigated in depth using XPS. The XPS survey spectrum of the material after adsorption (Fig. 7(a)) shows characteristic peaks of U 4d, U 4f, and U 5d, confirming the successful accumulation of U(VI) on the material surface [1]. Comparison of the high-resolution spectra before and after adsorption (Figs. 7(b)–7(e)) reveals systematic shifts of the characteristic peaks to higher energies in the C 1s, O 1s, N 1s, and W 4f spectra, indicating the stable coordination between U(VI) and the surface functional groups of PDA@PW_{12}. Notably, the peak area of the C–O group in the O 1s spectrum is considerably lower after adsorption, indicating the direct participation of surface hydroxyl functional groups in the coordination of U(VI) [50]. The U 4f high-resolution spectrum (Fig. 7(f)) further reveals changes in the valence state: the peaks at 382.13 and 393.03 eV were assigned to U(VI), whereas the peaks at 380.17 and 391.24 eV confirmed the presence of U(IV), indicating the partial reduction of U(VI) to U(IV) during adsorption [51]. Combined with the detection of W(V) species in the W 4f spectrum, this indicates that W(V) in PDA@PW_{12} acted as an electron donor to reduce U(VI) to U(IV). Notably, the redox reaction mediated by W(V) was non‑regenerative under the given experimental conditions, meaning that W(V) was irreversibly oxidized to W(VI) upon the reduction of U(VI) to U(IV). Consequently, the redox capacity was finite and limited by the initial content of W(V) in the composite. Therefore, this redox pathway mainly contributed to the initial rapid removal, working in synergy with the persistent coordination/complexation with the PDA matrix. In summary, the adsorption of U(VI) on PDA@PW_{12} proceeded through multiple synergistic mechanisms involving surface coordination and redox reactions (Fig. 8), which together substantially improved the overall uranium adsorption performance of the material.

3.7 DFT calculations

To verify the excellent adsorption performance of PDA@PW_{12} for uranyl ions (UO_2^{2+}), DFT-based first-principles calculations were performed to systematically compare the binding energies of UO_2^{2+} with PDA and PDA@PW_{12} (Figs. 9(a) and 9(b)). The calculations were performed using the Vienna *ab initio* simulation package with the Perdew–Burke–Ernzerhof form of the generalized gradient approximation for the exchange–correlation functional. To eliminate interactions between adjacent fragments under periodic boundary conditions, lattice parameters *a*, *b*, and *c* were all set to 30 Å. The plane–wave cutoff energy was set to 450 eV, with an electronic self-consistent iteration convergence criterion of 10^{-5} eV. Atomic structures were optimized until the Hellmann–Feynman forces were less than 0.01 eV/Å. A 1 × 1 × 1 *k*-point mesh was used for Brillouin zone sampling. The calculation results indicate that the binding energy of UO_2^{2+} with PDA is −3.17 eV, whereas the binding energy with PDA@PW_{12} is −10.87 eV (Table S3 in the ESM). This result theoretically confirms that the introduction of PW_{12} substantially strengthened interactions between the material and uranyl ions, providing a theoretical basis at the microscopic level for the superior uranium adsorption performance of PDA@PW_{12}.

4 Conclusions

Herein, a series of PDA@POM composites was successfully synthesized through in situ polymerization, with PDA@PW_{12} showing superior U(VI) adsorption performance. Systematic characterization and experimental results revealed that the

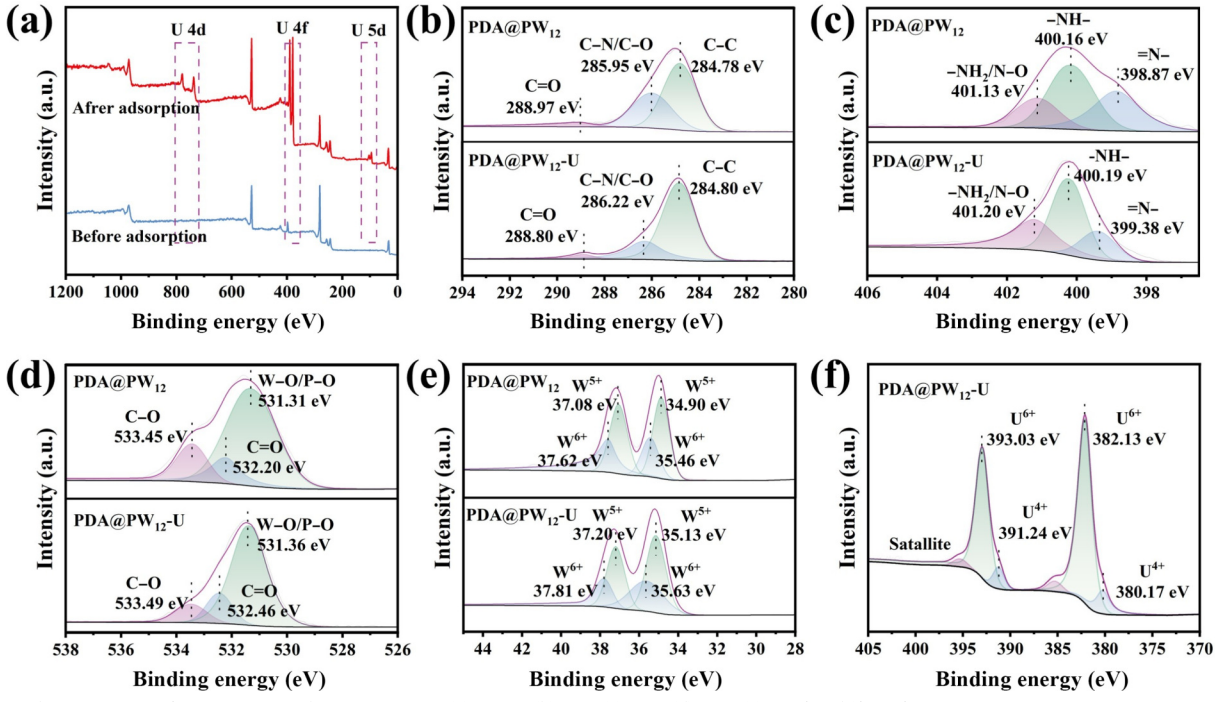

Figure 7 The XPS spectra of PDA@ PW_{12} and PDA@ PW_{12}-U: (a) survey, (b) C 1s, (c) N 1s, (d) O 1s, (e) W 4f, and (f) U 4f.

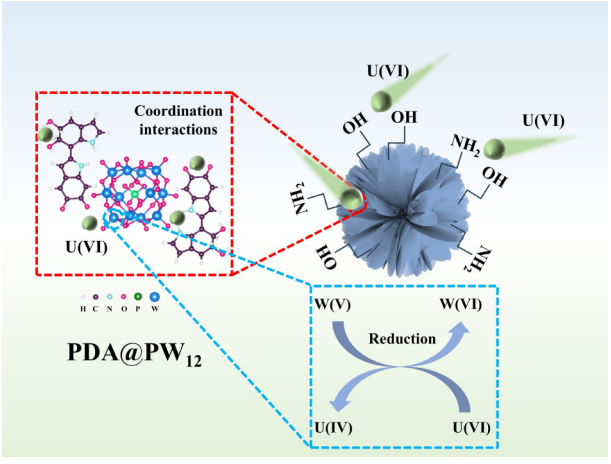

Figure 8 Schematic diagram of the mechanism for synergistic adsorption-reduction of U(VI) by PDA@PW_{12} composite microspheres.

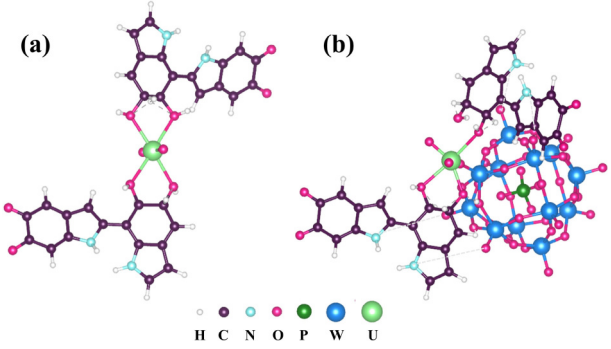

Figure 9 Adsorption and detailed model of (a) PDA with U(VI) and (b) PDA@PW_{12} with U(VI).

incorporation of PW_{12} inhibited PDA agglomeration, substantially increasing the specific surface area (48.069 m^2/g), and introduced abundant active sites. The adsorption of U(VI) on PDA@PW_{12} was determined to be monolayer chemisorption following the pseudo-second-order kinetic model, with a maximum saturation adsorption capacity of 720.1 mg/g at 318 K according to the Langmuir model. The adsorption mechanism involved the synergistic effects of surface complexation and redox reactions: surface functional groups (–OH and $–NH_2$) complexed with U(VI), whereas W^{5+} species within the composite acted as electron donors, partially reducing U(VI) to U(IV). DFT calculations further confirmed that the binding energy between PDA@PW_{12} and UO_2^{2+} is higher than that between PDA and UO_2^{2+} (−10.87 and −3.17 eV, respectively). Moreover, the composite exhibited excellent regeneration capability (93.3% desorption efficiency after 5 cycles), thermal stability (stable up to 350 °C), and selectivity for uranium. Thus, the present work provides a mechanistic understanding of the synergistic adsorption and reduction of U(VI) by PDA@PW_{12} and highlights its potential for practical applications in uranium extraction and recovery.

Electronic Supplementary Material: Supplementary material (characterization techniques, data analysis, N_2 adsorption–desorption isotherms, FTIR, XPS survey spectra, adsorption capacities toward U(VI) of some composite adsorbents, TGA curves, SEM images, the constants of Langmuir and Freundlich model) is available in the online version of this article at https://doi.org/10.26599/POM.2026.9140119.

Data availability

All data needed to support the conclusions in the paper are presented in the manuscript and the Electronic Supplementary Material. Additional data related to this paper may be requested from the corresponding author upon request.

Acknowledgements

This work was financially supported by the Natural Science Foundation of China (No. 22071018) and the Science and Technology Research Project of Jilin Educational Committee (No. JJKH20261699KJ). Authors dedicate this article to Professor Lin Xu of Northeast Normal University, honoring his pioneering contributions in Polyoxometalates Chemistry on the occasion of his 70th birthday.

Declaration of competing interest

The authors have no competing interests to declare that are relevant to the content of this article.

Author contribution statement

Y. L., L. M. Z., D. H. C., X. Y. and F. Y. L.: Project administration and writing manuscript. X. L. and K. Y. C.: Experimental design and data collection. Y. L. and F. Y. L.: Data curation. All the authors have approved the final manuscript.

Use of AI statement

During the preparation of this work, the authors used DeepSeek in order to revise the manuscript. After using this tool, the authors reviewed and edited the content as needed and take full responsibility for the content of the publication.

References

[1] Chen, D. Y.; Sun, M. F.; Zhao, X. Y.; Shi, M. S.; Fu, X. Y.; Hu, W.; Zhao, R. High-efficiency and economical uranium extraction from seawater with easily prepared supramolecular complexes. *J. Colloid. Interface Sci.* **2024**, *668*, 343–351.

[2] Chen, D. Y.; Li, Y.; Zhao, X. Y.; Shi, M. S.; Shi, X. Y.; Zhao, R.; Zhu, G. S. Self-standing porous aromatic framework electrodes for efficient electrochemical uranium extraction. *ACS Cent. Sci.* **2023**, *9*, 2326–2332.

[3] Xie, Y.; Liu, Z. Y.; Geng, Y. Y.; Li, H.; Wang, N.; Song, Y. P.; Wang, X. L.; Chen, J.; Wang, J. C.; Ma, S. Q. et al. Uranium extraction from seawater: Material design, emerging technologies and marine engineering. *Chem. Soc. Rev.* **2023**, *52*, 97–162.

[4] Ma, X. J.; Meihaus, K. R.; Yang, Y. J.; Zheng, Y.; Cui, F. C.; Li, J. X.; Zhao, Y. Q.; Jiang, B.; Yuan, Y.; Long, J. R. et al. Photocatalytic extraction of uranium from seawater using covalent organic framework nanowires. *J. Am. Chem. Soc.* **2024**, *146*, 23566–23573.

[5] Zhang, D.; Fang, L.; Liu, L. J.; Zhao, B.; Hu, B. W.; Yu, S. J.; Wang, X. K. Uranium extraction from seawater by novel materials: A review. *Sep. Purif. Technol.* **2023**, *320*, 124204.

[6] Pei, H. N.; Dong, Z. M.; Li, Z. F.; Huang, J.; Jiang, Y. P.; Li, Z. J.; Xu, L.; Cao, X. H.; Liu, Y. H.; Zhang, Z. B. et al. Synergistic effect of homojunction and Ohmic junctions in CdS boosting spatial charge separation for U(VI) photoreduction. *Nano Res.* **2024**, *17*, 6849–6859.

[7] Zhu, W. C.; Li, X.; Wang, D. J.; Fu, F.; Liang, Y. C. Advanced photocatalytic uranium extraction strategies: Progress, challenges, and prospects. *Nanomaterials* **2023**, *13*, 2005.

[8] Liu, Y. L.; Ai, K. L.; Lu, L. H. Polydopamine and its derivative materials: Synthesis and promising applications in energy, environmental, and biomedical fields. *Chem. Rev.* **2014**, *114*, 5057–5115.

[9] Zhang, Q.; Chen, Z. S.; Li, J. G.; He, X. C.; Peng, W.; Yan, C. P.; Huang, G. L. Mussel inspired synthesis of U6N@phos-PDA composite adsorbent for the efficient separation of U(VI). *J. Mol. Liq.* **2024**, *413*, 125946.

[10] Zhang, J. F.; Jiang, Y. F.; You, M.; Zhao, J.; Xue, S. W.; Fang, H. X.; Wei, Y. J.; Sun, Z. M.; Zeng, T.; Wan, Z. Q. et al. Polydopamine-modified coal fly ash composite electrodes for improved electroadsorption of uranium. *J. Water Process Eng.* **2025**, *72*, 107612.

[11] Wu, F. C.; Pu, N.; Ye, G.; Sun, T. X.; Wang, Z.; Song, Y.; Wang, W. Q.; Huo, X. M.; Lu, Y. X.; Chen, J. Performance and mechanism of uranium adsorption from seawater to poly(dopamine)-inspired sorbents. *Environ. Sci. Technol.* **2017**, *51*, 4606–4614.

[12] Zhang, J. Y.; Song, Y. T.; Yang, J.; Pei, W. Y.; Ma, J. F. A series of four-substituted polyoxometalate-thiacalix[4]arene-based materials for the efficient photocatalytic reduction of Cr(VI). *Inorg. Chem. Front.* **2024**, *11*, 3011–3020.

[13] Lin, X. L.; Hu, Q. L.; Tan, K. X.; Chen, X. J.; Yang, G. P.; Wei, Y. G. Two Mn (II)-bridged silverton-type $[UMo_{12}O_{42}]^{8-}$ polyoxometalates with catalytic activity for the synthesis of pyrazoles. *Inorg. Chem.* **2024**, *63*, 12469–12474.

[14] Hu, B.; Liu, B. L.; Pan, Q. Q.; Ren, H. D.; Yu, F. Y.; Du, Q. C.; Li, Y. G.; Zang, H. Y. Structural effects in polyoxometalate-based supramolecular assemblies for enhanced proton conduction. *Angew. Chem.* **2025**, *138*, e17958.

[15] Dong, Z. M.; Zeng, D. L.; Li, Z. F.; Chen, J. J.; Wang, Y. Q.; Cao, X. H.; Yang, G. P.; Zhang, Z. B.; Liu, Y. H.; Yang, F. Polyoxometalate-encapsulated metal-organic frameworks for photocatalytic uranium isolation. *Chem. Sci.* **2024**, *15*, 19126–19135.

[16] Yang, G. P.; Li, K.; Hu, C. W. Recent advances in uranium-containing polyoxometalates. *Inorg. Chem. Front.* **2022**, *9*, 5408–5433.

[17] Liu, B. L.; Hu, B.; Du, J.; Cheng, D. M.; Zang, H. Y.; Ge, X.; Tan, H. Q.; Wang, Y. H.; Duan, X. Z.; Jin, Z. et al. Precise molecular-level modification of nafion with bismuth oxide clusters for high-performance proton-exchange membranes. *Angew. Chem.* **2021**, *133*, 6141–6150.

[18] Liu, C. L.; Xuan, K.; Guo, Y. P.; Jiang, H.; Ma, W. J.; Wang, X. G.; Zhou, Z. K.; Li, J.; Guo, Y. D. Highly efficient capture of uranium (VI) from wastewater by urchin-like $W_{18}O_{49}$: Insights to performance-dependence on active sites. *Rare Met.* **2025**, *44*, 6786–6800.

[19] Zhang, C. H.; Zhao, M. M.; Zou, H. J.; Zhang, X. M.; Sheng, R. T.; Zhang, Y.; Zhang, B. Y.; Li, C. Y.; Qi, Y. F. An enhanced antibacterial nanoflowers AgPW@PDA@Nisin constructed from polyoxometalate and nisin. *J. Inorg. Biochem.* **2020**, *212*, 111212.

[20] Hu, B.; Du, Q. C.; Yang, Y.; Li, D. D.; Fu, J. W.; Liu, B. L.; Zang, H. Y.; Li, Y. G.; Xie, H. M.; Su, Z. M. Facile construction of polyoxometalate-modified polyaryletherketone-based hybrid membranes with enhanced proton conductivity. *Polyoxometalates* **2025**, *4*, 9140079.

[21] Han, X. N.; Yu, J. W.; Chen, Y. D.; Qu, H.; Ruan, Z. N.; Lin, M. J.; Hou, J. H.; Liao, Q. Polydopamine-polyoxometalate composites in neutral pH enable high-efficiency and ultra-stable organic solar cells via mutual doping mechanism. *Adv. Mater.* **2025**, *37*, e12965.

[22] Fu, J. W.; Yang, Y.; Du, Q. C.; Liu, B. L.; Sun, H. Y.; Hu, B.; Su, Z. M. Interfacial engineering architecture of isatin-derived polymer-tethered polyoxometalates and their application in sulfonated poly(aryl ether ketone) proton exchange membranes. *ACS Appl. Mater. Interfaces* **2025**, *17*, 70827–70838.

[23] Lv, R. J.; Zhang, X. M.; Sun, R. M.; Chen, L. X.; Zhang, Y.; Sheng, R. T.; Du, T.; Li, Y. H.; Qi, Y. F. Hierarchical micro-nanostructures from polyoxometalates and polydopamine: Characterization, electrochemical and intrinsic peroxidase-like properties. *Particuology* **2022**, *64*, 178–185.

[24] Wang, M. M.; Chen, S.; Yu, Y. L.; Wang, J. H. Novel Ti^{4+}-chelated polyoxometalate/polydopamine composite microspheres for highly selective isolation and enrichment of phosphoproteins. *ACS Appl. Mater. Interfaces* **2019**, *11*, 37471–37478.

[25] Xing, C. L.; Ma, M.; Chang, J. N.; Ji, Z.; Wang, P. F.; Sun, L.; Li, S. J.; Li, M. X. Polyoxometalate anchored zinc oxide nanocomposite as a highly effective photocatalyst and bactericide for wastewater decontamination. *Chem. Eng. J.* **2023**, *464*, 142632.

[26] Zou, X. Y.; Shi, R.; Zhang, Z. J.; Fu, G. Y.; Li, L.; Yu, L.; Tian, Y. R.; Luo, F. Calcined ZnTi-layered double hydroxide intercalated with $H_3PW_{12}O_{40}$ with efficiently photocatalytic and adsorption performances. *Chem.—Eur. J.* **2021**, *27*, 16670–16681.

[27] Fu, J. W.; Chen, Z. H.; Wang, M. H.; Liu, S. J.; Zhang, J. H.; Zhang, J. N.; Han, R. P.; Xu, Q. Adsorption of methylene blue by a high-efficiency adsorbent (polydopamine microspheres): Kinetics, isotherm, thermodynamics and mechanism analysis. *Chem. Eng. J.* **2015**, *259*, 53–61.

[28] Shi, W. X.; Liu, Z. Y.; Zhang, Z. M. CdS-POM nanosheets for highly efficient visible-light-driven H_2 evolution. *Inorg. Chem. Front.* **2023**, *10*, 4534–4543.

[29] Chen, J. Q.; Gao, J. Z.; Lv, H. T.; Wen, Q. H.; Han, J. R.; Liu, P.; Yan, Y. D.; Xue, Y.; Ma, F. Q. Preparation of polydopamine-functionalized polyamidoxime membrane for uranium recovery from seawater. *Appl. Surf. Sci.* **2023**, *634*, 157604.

[30] Zhang, S.; Deng, S.; Bo, T.; Li, Y. L.; Zhao, J. Y.; Wang, Y. C.; Jiang, H.; Li, X. Y.; Liu, Y. H. A bio-inspired PDA@MoS_2 electrode with high conductivity and excellent antibacterial properties for selective and efficient uranium recovery via capacitive deionization. *Chem. Eng. J.* **2025**, *514*, 163199.

[31] Kang, Q. L.; Lai, D. W.; Su, M. F.; Xiong, B. R.; Tang, W. Y.; Lu, Q. Y.; Gao, F. Tailored dodecahedral polyoxometalates nanoframes with *in situ* encapsulated Co, N, C for oxygen evolution reaction. *Chem. Eng. J.* **2022**, *430*, 133116.

[32] Yang, B.; Zhao, J. J.; Zhang, C.; Guo, S. S.; Chen, Y. L.; Wang, Y.; Huang, X. X.; Zeng, Q. Y. Ultra-high capacity and selectivity for uranium fixation by carbon nanosphere supported hydroxyapatite nanorod adsorbent. *J. Colloid Interface Sci.* **2025**, *688*, 478–489.

[33] Liu, T.; Xie, Z. J.; Chen, M. W.; Tang, S.; Liu, Y. J.; Wang, J.; Zhang, R. Q.; Wang, H.; Guo, X.; Gu, A. P. et al. Mussel-inspired dual-crosslinked polyamidoxime photothermal hydrogel with enhanced mechanical strength for highly efficient and selective uranium extraction from seawater. *Chem. Eng. J.* **2022**, *430*, 133182.

[34] Chen, C. C.; Liu, X.; Tian, X. Y.; Feng, J. Q.; Liu, Y. J.; Song, M. J.; Zhu, W. K.; Zhang, Y. The efficient uptake of uranium by amine-functionalized β-cyclodextrin supported fly ash composite from polluted water. *Sci. Total Environ.* **2024**, *927*, 172342.

[35] Li, L. Y.; Li, H.; Lin, M. Z.; Wen, J.; Hu, S. Effects of chain conformation on uranium adsorption performance of amidoxime adsorbents. *Sep. Purif. Technol.* **2023**, *307*, 122777.

[36] Chen, D. Y.; Zhao, X. Y.; Shi, M. S.; Fu, X. Y.; Hu, W.; Shi, X. Y.; Zhao, R.; Zhu, G. S. Enhanced and selective uranium extraction onto electrospun nanofibers by regulating the functional groups and photothermal conversion performance. *Chem. Eng. J.* **2024**, *480*, 148108.

[37] Li, Z. J.; Tuo, K.; Wang, W. F.; Wei, Q. F.; Li, K. N.; Wang, Y. G. Construction of oxime functionalized mesoporous polydopamine

spheres based on emulsion-induced interface assembly approach for efficient extraction of uranium. *Appl. Surf. Sci.* **2025**, *680*, 161343.
[38] Wang, Y.; Zhang, Y.; Liu, X. L.; Sun, S.; Qin, S. Y.; Huang, J. Q.; Chen, B. W. Polydopamine/β-cyclodextrin/coal fly ash composite for the highly efficient extraction of uranium from water environment. *J. Ind. Eng. Chem.* **2023**, *127*, 239–249.
[39] Dai, Z. R.; Sun, Y. S.; Zhang, H.; Ding, D. X.; Li, L. Rational synthesis of polyamidoxime/polydopamine-decorated graphene oxide composites for efficient uranium(VI) removal from mine radioactive wastewater. *Ind. Eng. Chem. Res.* **2019**, *58*, 19280–19291.
[40] Bliznyuk, V. N.; Kołacińska, K.; Pud, A. A.; Ogurtsov, N. A.; Noskov, Y. V.; Powell, B. A.; DeVol, T. A. High effectiveness of pure polydopamine in extraction of uranium and plutonium from groundwater and seawater. *RSC Adv.* **2019**, *9*, 30052–30063.
[41] Wu, F.; Li, H.; Tang, J.; Haleem, A.; Pan, J. M. Surface wettability guiding *in situ* cultivation engineering of hollow polymer nanospheres for persistent efficient uranium extraction. *J. Mater. Chem. A* **2023**, *11*, 26661–26671.
[42] Jiang, Z. Y.; Zhou, Y. Z.; Wang, W. S.; Yin, Z.; Zhao, M. Z.; Yu, L.; Ren, S. J.; Xiao, H.; Ma, Y. F. Strategically designed ternary nanohybrids of titanate nanosheet and polydopamine-coated carbon nanotubes for highly efficient enrichment of uranium(VI). *ACS Omega* **2024**, *9*, 49108–49120.
[43] Yang, H.; Ding, H. L.; Zhang, X. N.; Luo, X. G.; Zhang, Y. Immobilization of dopamine on *Aspergillus niger* microspheres (AM/PDA) and its effect on the U(VI) adsorption capacity in aqueous solutions. *Colloids Surf. A: Physicochem. Eng. Aspects.* **2019**, *583*, 123914.
[44] Ou, T.; Wu, Y. H.; Han, W. X.; Kong, L. J.; Song, G.; Chen, D. Y.; Su, M. H. Synthesis of thickness-controllable polydopamine modified halloysite nanotubes (HNTs@PDA) for uranium (VI) removal. *J. Hazard. Mater.* **2022**, *424*, 127208.
[45] Feng, J. H.; Cai, Y. W.; Wang, X. X.; Wang, X.; Zhu, M. Y.; Fang, M.; Liu, Z. H.; Tan, X. L. Designed core-shell Fe_3O_4@polydopamine for effectively removing uranium(VI) from aqueous solution. *Bull. Environ. Contam. Toxicol.* **2021**, *106*, 165–174.
[46] Zhou, Y. Z.; Li, Y.; Liu, D. X.; Liu, D. B.; Xu, L. D.; Liu, C. Adsorption optimization of uranium(VI) onto polydopamine and sodium titanate co-functionalized MWCNTs using response surface methodology and a modeling approach. *Colloids Surf. A: Physicochem. Eng. Aspects.* **2021**, *627*, 127145.
[47] Wang, Z.; Xu, C.; Lu, Y. X.; Wei, G. Y.; Ye, G.; Sun, T. X.; Chen, J. Microplasma electrochemistry controlled rapid preparation of fluorescent polydopamine nanoparticles and their application in uranium detection. *Chem. Eng. J.* **2018**, *344*, 480–486.
[48] Wang, C.; Gao, Z. X.; Zang, H. Y.; Dong, T. W.; Su, Z. M. Solid-state supercapacitors based on polyoxometalate-based crystalline materials modified with polyaniline. *Inorg. Chem. Front.* **2023**, *10*, 3641–3647.
[49] Liu, C. L.; Xu, Y. G.; Peng, Y. Y.; Wang, H. Q.; Chen, Y. X.; Zhang, Y. Dual Surface defects induced efficient interfacial electron transfer in S-scheme hollow ZnO@ZnS heterojunction for uranium (VI) removal. *Sep. Purif. Technol.* **2025**, *352*, 128172.
[50] Xu, L. Z.; Chen, Y. B.; Zhang, Y. Y.; Wang, M.; Wei, S. Y. Highly adherent $Ti_3C_2T_x$ nanosheet-loaded amidoxime polyacrylonitrile composite membrane for uranium extraction. *Sep. Purif. Technol.* **2024**, *331*, 125613.
[51] Mai, S. S.; Hsiao, K. Y.; Yang, Y. C.; Lu, Y. R.; Lu, M. Y.; Hsieh, Y. Y.; Chang, C. B.; Tuan, H. Y. Synchronous regulation of schottky/p-n dual junction in Prussian blue-derived Janus heterostructures: A path to ultrafast long life potassium ion batteries. *Chem. Eng. J.* **2023**, *474*, 145992.

Yu Liu is a Ph.D. student in the College of Chemistry at Northeast Normal University. His research interests primarily focus on the synthesis of polyoxometalates and their applications in catalytic chemistry.

Limin Zhang is a Master's candidate in the College of Chemistry at Northeast Normal University. Her research focuses on the design, synthesis, and catalytic performance optimization of counter electrodes for quantum dot-sensitized solar cells.

Donghui Cui is a Ph.D. candidate in the College of Chemistry at Northeast Normal University. His research primarily focuses on the modification of carbon nitride materials and their photocatalytic nitrogen fixation performance. He has published multiple research papers in journals such as JCIS, SPT, Small, and ACS AMI.

Xue Yang is a Ph.D. candidate in the College of Chemistry at Northeast Normal University. Her research focuses on the controlled preparation of bismuth-based materials and their application in photocatalytic nitrogen fixation.

Xiao Liang is a Master's candidate in the College of Chemistry at Northeast Normal University. His research focuses on the application and performance optimization of sulfide materials in catalytic hydrogen production.

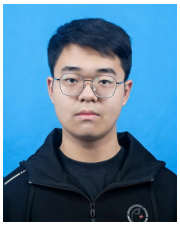

Keyu Chen is an undergraduate student in the College of Chemistry at Northeast Normal University. His research interests primarily focus on the synthesis of polyoxometalates.

Fengyan Li received her Ph.D. degree under the direction of Professor Lin Xu from Northeast Normal University (NENU) in 2008. During this time, she worked at University of Glasgow (UK) as a Joint training Ph.D. student in 2007. After a visiting scholar experience (2017-2018) at University of California, Riverside (USA), she works as a professor at the Key Laboratory of Polyoxometalate and Reticular Material Chemistry of Ministry of Education, NENU. Her current research interests include the synthesis of POM-based functional materials and their applications in the fields of energy storage and energy conversion, in particular, their uses in photocatalytic nitrogen fixation, photocatalytic H_2 evolution and photocatalytic uranium removal.